IOPscience iopscience.iop.org

Home Search Collections Journals About Contact us My IOPscience

The spatial–temporal evolution of the electron density and temperature for a nanosecond microdischarge

This content has been downloaded from IOPscience. Please scroll down to see the full text.

2013 J. Phys. D: Appl. Phys. 46 464011

(http://iopscience.iop.org/0022-3727/46/46/464011)

View the table of contents for this issue, or go to the journal homepage for more

Download details:

IP Address: 129.180.1.217
This content was downloaded on 23/10/2014 at 10:26

Please note that terms and conditions apply.

J. Phys. D: Appl. Phys. **46** (2013) 464011 (10pp) doi:10.1088/0022-3727/46/46/464011

The spatial–temporal evolution of the electron density and temperature for a nanosecond microdischarge

Bang-Dou Huang, Xi-Ming Zhu, Keisuke Takashima and Yi-Kang Pu

Department of Engineering Physics, Tsinghua University, Beijing 100084, People's Republic of China

Received 31 March 2013, in final form 1 July 2013
Published 31 October 2013
Online at stacks.iop.org/JPhysD/46/464011

Abstract

The spatial–temporal evolution of the electron density (n_e) and the electron temperature (T_e) in a nanosecond microdischarge with a pin-to-pin electrode configuration is investigated by optical emission spectroscopy, using Stark broadening and collisional–radiative models. The measurement is focused on the evolution of the axial distribution (between the two electrodes) of both n_e and T_e. It is found that the time evolution of n_e profile can be divided into three phases: (1) during the pulse-on period (breakdown to ∼16 ns), a very non-uniform profile develops under the influence of strong external electric field; (2) during the early afterglow period (∼16 ns to ∼ one hundred nanoseconds), the n_e decreases and its profile gets more uniform due to diffusion; (1) during the late afterglow period (∼100 ns to ∼600 ns), the electron density profile becomes non-uniform again with its highest value near the power electrode. This is possibly caused by the secondary electron emission due to the ion impact onto the power electrode, which is biased negatively by the external power supply at this time. During the pulse-on period, the behaviour of the T_e is similar to that of the n_e, although its magnitude of the variation across the electrodes and with time is much smaller. In the afterglow period, the residue power input tends to slow down the electron cooling, especially in the region near the power electrode.

(Some figures may appear in colour only in the online journal)

1. Introduction

Due to their high ionization degree and low gas temperature (T_g), nanosecond microdischarges can generate active species efficiently. Their potential applications include light sources [1, 2], material processing [3] and bio-medical treatment [4, 5]. However, their discharge physics needs to be investigated, not only because it is a very interesting topic of research but it can also help the development of high-performance commercial products.

In order to understand the discharge physics of the nanosecond microplasmas, it is necessary to have quantitative information on certain important discharge parameters, such as the electron density and the electron temperature. Depending on the electrode configuration, both of these two parameters can have highly non-uniform spatial profiles. In addition, these spatial profiles can evolve with time in both pulse-on and pulse-off phases. Therefore, it is desirable to be able to measure the spatial distribution of both n_e and T_e and their evolution with time.

To measure the n_e and T_e for such a microplasma, optical emission spectroscopy (OES) is a good candidate. First of all, it is non-intrusive. This is very important for the diagnostics of high- pressure microdischarges as any probe can act as an electrode and significantly disturb the discharge. Secondly, OES diagnostics are relatively easy and inexpensive to set it up. If the OES system is equipped with an intensified charge-coupled device (ICCD) camera, temporal resolution up to several nanoseconds can be achieved. Furthermore, if the OES is equipped with a proper optical imaging system, spatial resolution up to micrometres can be realized [6, 7]. All of these features are essential for diagnosing pulsed microplasmas, whose discharge parameters usually vary with a time scale of nanoseconds and a length scale of micrometres.

The technique of obtaining the n_e from the Stark broadening of emission lines has been used for many kinds of discharges, such as dc- [8–10], rf- [11] and microwave-coupled microplasmas [12, 13], dielectric barrier discharges (DBDs) [14] and laser induced microplasmas [15, 16]. The

 © 2013 IOP Publishing Ltd Printed in the UK & the USA

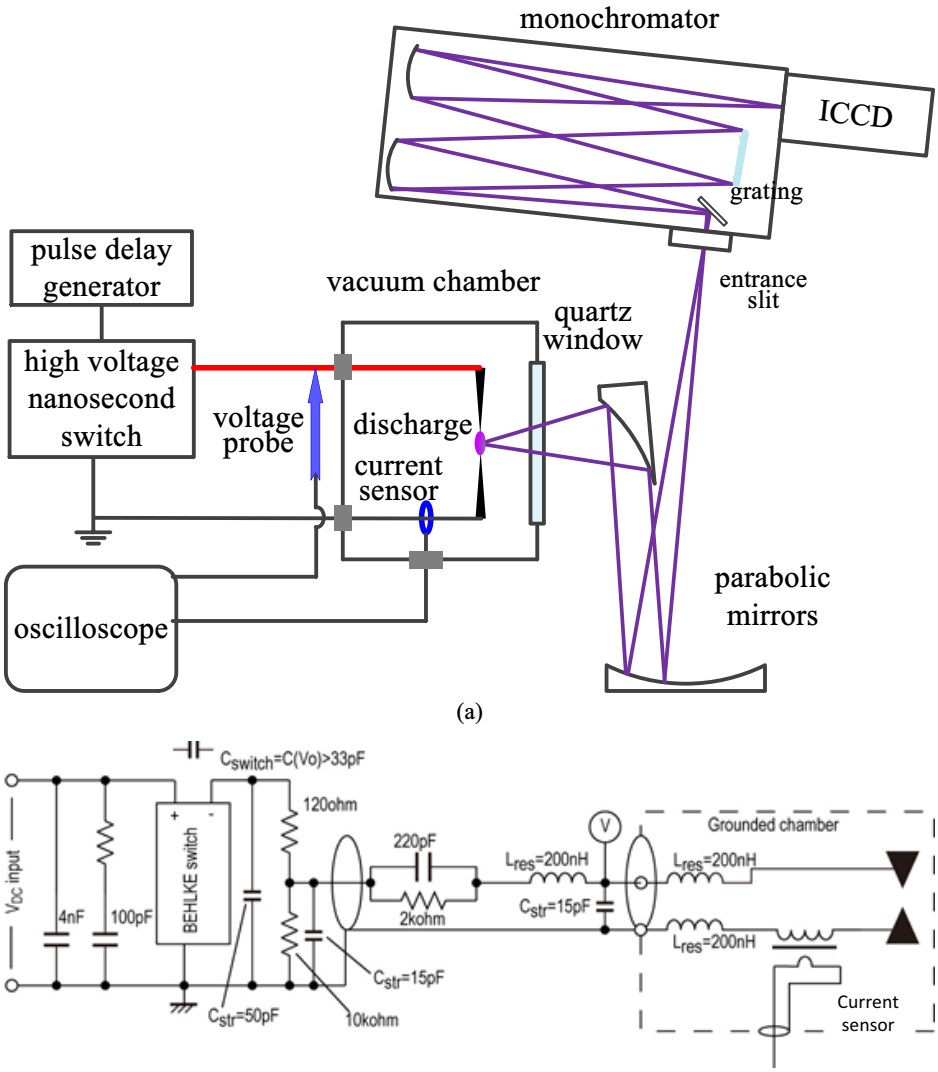

Figure 1. (*a*) The experimental setup. (*b*) The equivalent circuit including both the pulse generator and the discharge setup.

Stark broadening of hydrogen Balmer series, which usually has a larger broadening than other emission lines, can be used to obtain the n_e with a reasonable accuracy when its value is higher than $\sim 10^{14}$ cm^{-3} [17].

Assuming the electron energy distribution function (EEDF) is a Maxwellian, the measured line ratio combined with a collisional–radiative (CR) model can be used to determine the electron temperature for high-pressure discharges. Even though collisions with neutral species can strongly affect the excited species kinetics and the electron temperature is quite low for these high-pressure discharges, its variation can still have a significant effect on certain line ratios when the n_e is high enough. A simple CR model used for electron temperature determination in helium and argon mixture discharge is described in detail in section 3.3.1.

In this work, for a pin-to-pin nanosecond discharge in helium with 1% argon and 0.01% hydrogen gas mixture at one atmospheric pressure, spatially and temporally resolved measurement of the n_e and the T_e is performed. The obtained results clearly show how the discharge evolves in time with distinct phases. In addition, this is a continuation of an earlier work [17], where it was predicted that a non-uniform n_e distribution leads to the necessity of a 'double Voigt' fitting of a volume integrated spectral line profile. Our spatially resolved measurement result confirms such a prediction.

2. Experiment

As shown in figure 1(*a*), the nanosecond power source consists of a nanosecond switch (Behlke, HTS 331-06), a controller for the switch (home-made), and a dc high-voltage (HV) power supply (Spellman, PTV350). The positive HV output from the switch is connected to one of the pins (the HV/powered electrode) inside a stainless steel vacuum chamber. The distance between the tips of the two pins is approximately 0.8 mm. The voltage waveform on the HV electrode and the current waveform are measured with an HV probe (Tektronix, P6015A) and a current sensor (Pearson 2877), respectively, and these data are recorded by an oscilloscope (LeCroy, 104MXi).

A digital pulse delay generator (Stanford Research System, DG645) is used to generate the trigger signal and the repetition frequency is 200 Hz. A circuit for both the pulse generator and the discharge setup is given in figure 1(*b*).

The atmospheric pressure discharge is ignited in helium mixed with 1% argon and 0.01% hydrogen. In this way, helium, argon and hydrogen emission lines of interest can be collected with a satisfactory signal-to-noise ratio over a time period of several hundred nanoseconds (well into the late afterglow period).

The optical emission from the discharge is collected with an imaging system, which consists of one parabolic mirror (focal length 60 cm, diameter 15 cm) and one 90° off-axis parabolic mirror (focal length 20 cm, diameter 5 cm). The discharge is imaged onto the entrance slit of the monochromator (Zolix, Lamda500, focal length 0.5 m, slit width 50 μm). The spectra are taken with an ICCD camera (Princeton Instruments, PI-MAX2). We use three different gratings in the monochromator for the spectrum measurement. The first grating (1200 g mm^{-1}, blaze wavelength 600 nm) is used to record the H_β (486.1 nm), H_α (656.3 nm), helium 587.56 nm ($3\ ^3D \rightarrow 2\ ^3P$) and argon 750.39 nm ($2p_1 \rightarrow 1s_2$, in Paschen's notation) lines. The second one (2400 g mm^{-1}, blaze wavelength 240 nm) is used to record the N_2 second positive band ($C\ ^3\Pi_u$, $v = 0 \rightarrow B\ ^3\Pi_g$, $v' = 0$, 335.5–337.5 nm). The third one (500 g mm^{-1}, blaze wavelength 330 nm) is also used to record the H_β (486.1 nm) line when the line width is large at the beginning of the discharge. The spectral response of the entire system is calibrated with a tungsten halogen lamp (Newport, 63355).

The resolution of the optical system is obtained from the emission lines of the low-pressure mercury, neon and argon lamps. With each grating, the instrumental broadening profiles fit well with a Gaussian profile. The resolutions of the optical system with the first, second and third grating are about 0.1 nm, 0.05 nm and 0.25 nm, respectively.

As the effective resolution of the ICCD is about $40 \times 40\ \mu m^2$ and the magnification factor of the imaging system is about 3, each pixel corresponds to $\sim 13 \times 13\ \mu m^2$ inside the discharge. Considering the aberration and diffraction limitation of the optical system, it is believed that the entire setup can provide a spatial resolution better than 20 μm along the axis of the two pins [7, 18].

Figure 2 shows a typical image of the discharge, taken with the imaging system and an ICCD camera (without the monochromator) at 10 ns after the breakdown occurs (gate width 2 ns). It can be seen that the emission is most intense near the HV electrode and it decreases along the gap to the ground electrode.

3. Results and discussion

3.1. Voltage and current waveforms

Figure 3 shows the voltage, current and power waveforms of the discharge over a time period of ~400 ns.

The voltage (blue line) starts to increase at ~−20 ns and reaches to its peak value (~4.3 kV) at 0 ns) with a rate of

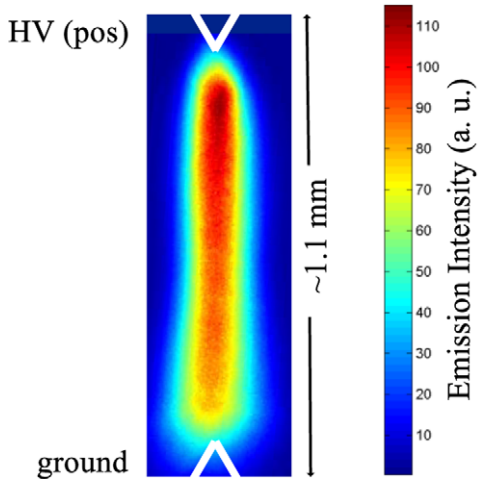

Figure 2. Spatially resolved emission intensity of the discharge. This image is taken at 10 ns after the breakdown and the gate width of the ICCD is 2 ns. The white triangles in the image represent the edge of the electrode. 'HV (pos)' is the positive HV electrode and 'ground' is the ground electrode.

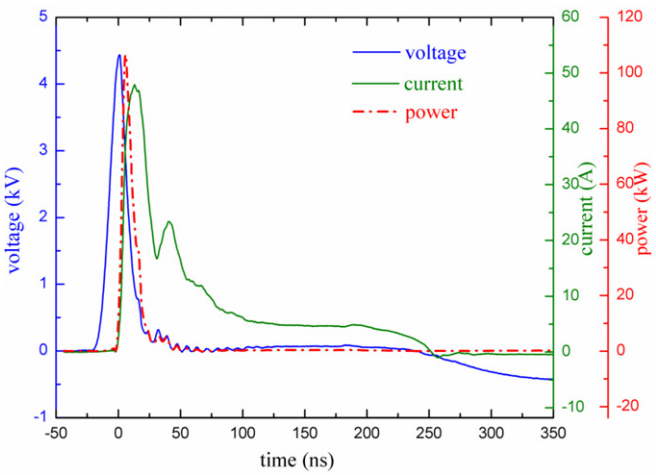

Figure 3. Voltage (blue line) and current (green line) waveforms. The gas pressure is 760 Torr with helium +1% argon+0.01% hydrogen mixture. The red curve is the instantaneous power from the product of voltage and current.

~0.2 kV ns^{-1}. A few nanoseconds before that, the breakdown occurs and the current (green line) starts to increase. Notice that, in this experimental setup, the displacement current is negligible since the stray capacitance of the discharge system (the 'load') is very small (~0.3 pF).

As the current increases, the coupling power (red line) to the load starts to increase and then decreases quickly from 6 to 25 ns due to the drastic reduction of the voltage. This voltage drop is mainly caused by the decrease of the load impedance. As the breakdown develops, this impedance (several ohms) can be much lower than the output impedance (~100 Ω) of the nanosecond power source.

When the voltage decreases to around zero (~50 ns), the voltage ringing with a frequency about 100 MHz can be seen in figure 3. This frequency is determined by the stray capacitance and the residual inductance of the cables and the pulse generator. At the same time, the current waveform shows

some fluctuation with a lower frequency (~40 MHz). This fluctuation time scale is controlled by the residual inductances and the capacitance in the power source. Notice that the current decay time (~20 ns) is also controlled by this capacitance.

From ~60 to ~120 ns, the voltage increases slowly to ~50 V, while the current continues to decrease. This is due to the decay of the discharge, which results in an increase of the load impedance. Later, both the voltage and the current remain more or less constant until ~200 ns.

Even though the BEHLKE switch is turned off at ~200 ns, the remaining charge in the circuit continues to provide heating to the discharge. In fact, the voltage experiences a slow decrease and then changes to negative at ~240 ns. At 350 ns, the voltage at the power electrode has reached a value of ~−400 V, with a discharge current of ~0.5 A. This power input provides dominant heating to the electrons compared with the collisional processes and tends to slow down the electron cooling (more discussion can be found in section 3.3). On the other hand, it can be estimated that, the plasma impedance is approximately 20 Ω at 350 ns, giving a voltage drop of ~10 V. Therefore, most of the ~400 V is across the cathode sheath, which is capable of producing energetic ions. After that, the plasma continues to decay and the corresponding load impedance continues to increase, leading to a fairly long decay time of the negative voltage (~1 μs, not shown).

3.2. Evolution of the n_e

The temporal–spatial evolution of the n_e is shown in figures 4(*a*)–(*c*). The n_e is obtained from the full-width half-maximum (FWHM) of the Stark broadening of the H_α line, as described in [17].

In figure 4(*a*), at 8 ns, the n_e near the HV electrode (~2×10^{16} cm^{-3}) is about three times the value near the ground electrode (~6×10^{15} cm^{-3}). It is possible that the ionization process near the positive HV electrode (with a stronger local field) is much more intensive than that near the ground electrode. During a later time period (8–16 ns), driven by the external field, a much more non-uniform distribution of the electron density develops and the peak value has been increased by one order of magnitude (to ~1.5×10^{17} cm^{-3}). Notice that the peak is located about a few tens of micrometres away from the HV electrode, not at the location closest to it. This is due to the strong electron loss in the region near the HV electrode (a sheath-like region). At 30 ns, the same trend continues and the n_e has a peak value of ~2.3×10^{17} cm^{-3} (the maximum n_e in the discharge), at a location of the peak further away from the HV electrode (about 0.1 mm).

When the pulse is off (~35 ns), even though the n_e profile looks similar to that at 30 ns, it is actually more uniform, with a significant decrease of its peak value (figure 4(*b*)). In fact, the n_e profile keeps getting more uniform until 100 ns (figure 4(*c*)). During this time period, the voltage on the HV electrode is very low (~50 V) and the external heating field is much reduced. As a result, the ionization process is very weak. On the other hand, the transport of the electrons along the axial direction and the strong diffusion to the HV electrode caused by the sharp density gradient will lead to a more uniform electron density profile between the two electrodes.

However, at a later time ($\geqslant$ 200 ns), the plasma becomes more non-uniform again, despite the fact that the n_e keeps decreasing at all locations. At 400 ns, in particular, the n_e profile can be fitted fairly well with a straight line, with its maximum near the HV electrode (figure 4(*d*)). This suggests the n_e profile can be considered as a solution of a diffusion equation with no volume source term. At this time, the HV electrode voltage is about −400 V (not shown), which leads to energetic ion impact onto the electrode and this can induce secondary electron emission. These secondary electrons, in our opinion, may have a significant contribution to the total current near the HV electrode (a cathode) and are the new source of ionization. This effect can last up to several hundred nanoseconds due to the continuous negative biasing and ion impact.

The evolution of the n_e profile can be revealed more clearly by defining the following two non-uniform parameters:

$$R_{\text{max to min}} = \frac{n_{e,\max}}{n_{e,\min}} \tag{1}$$

and

$$R_{\text{HV to GND}} = \frac{n_{e,\text{HV}}}{n_{e,\text{GND}}} \tag{2}$$

Here, $n_{e,\max}$ and $n_{e,\min}$ are the maximum and minimum value of the n_e, respectively. $n_{e,\text{HV}}$ and $n_{e,\text{GND}}$ are the n_e closest to the HV electrode and that closest to the ground electrode, respectively. The variation of both parameters versus time is shown in figure 4(*e*), where it can be seen that the $R_{\text{max to min}}$ reaches its maximum at 16 ns and its minimum at ~100 ns, meanwhile, the $R_{\text{HV to GND}}$ does not change significantly before ~20 ns, after which the $R_{\text{HV to GND}}$ has the same trend as the $R_{\text{max to min}}$.

During the first phase of the discharge (before 16 ns), the development of non-uniform profiles is solely due to the strong (and local) ionization process driven by the external field near the HV electrode. After 16 ns, as the voltage continues to decrease (~100 V at 30 ns), the dominant process changes to diffusion, so the plasma is getting more uniform. We call this the second phase of the discharge. In the late afterglow, the secondary electron emission from the HV electrode makes the n_e non-uniform again, as discussed above. This is the third phase of the discharge.

3.3. Evolution of the T_e

3.3.1. The CR model. A simple CR model for helium/argon mixture discharges is used to estimate the electron temperature from the line ratio of helium 587.56 nm ($3\,^3\text{D} \rightarrow 2\,^3\text{P}$) to argon 750.39 nm ($2p_1 \rightarrow 1s_2$, in Paschen's notation). The lowest 10 excited levels of helium ($n = 2, n = 3$) and the lowest 14 excited levels of argon (1s, 2p) are incorporated (table 1) in this model, which includes electron excitation and population transfer,

$$\begin{aligned} &e+He_g \leftrightarrow e+He_i \\ &e+He_i \leftrightarrow e+He_j \\ &e+Ar_g \leftrightarrow e+Ar_i \\ &e+Ar_i \leftrightarrow e+Ar_j \end{aligned} \tag{3}$$

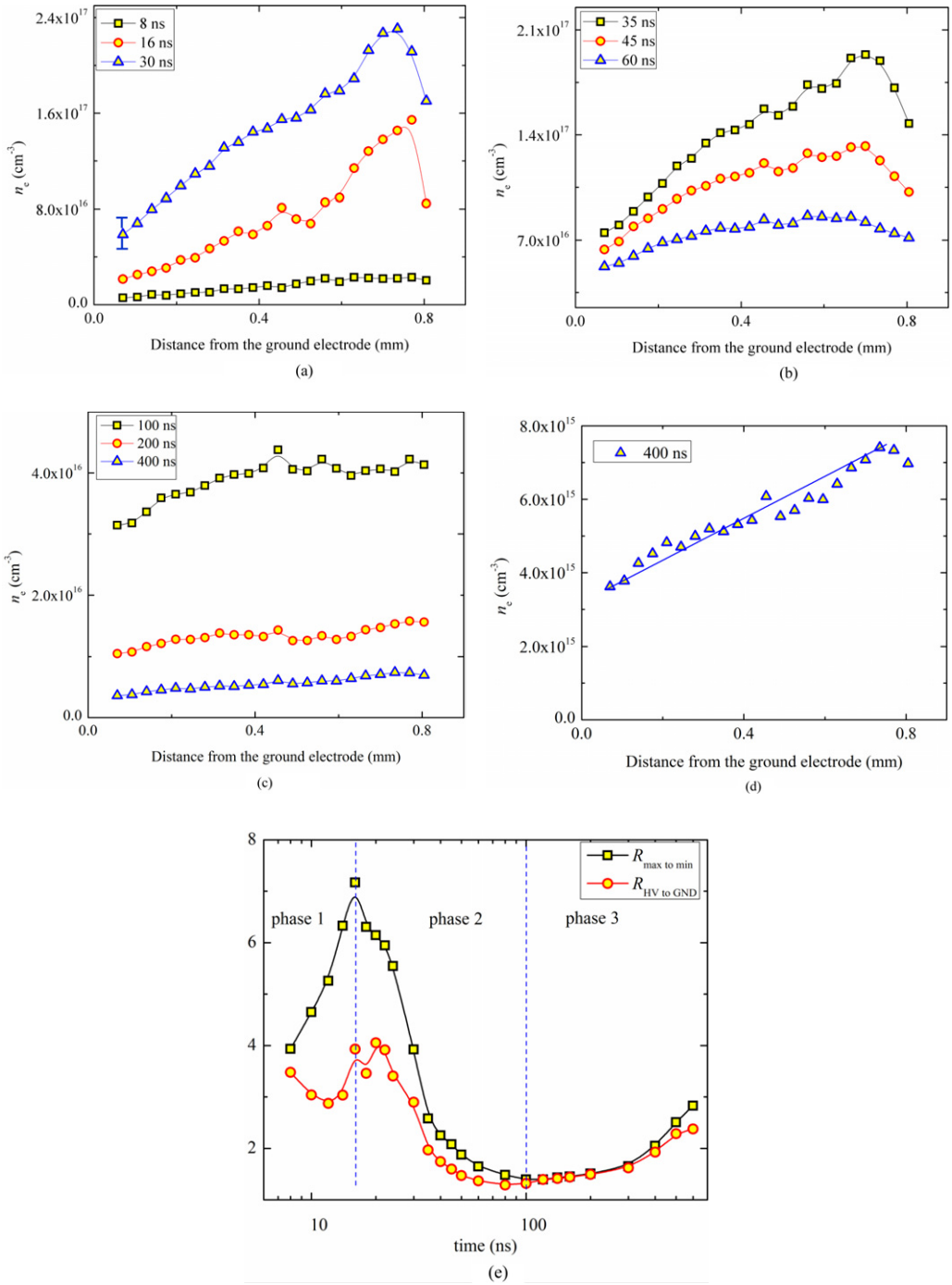

Figure 4. (*a*) (*b*) (*c*) Temporal–spatial evolution of the n_e. The gate width of the ICCD is 2 ns for the data at 8 ns and 16 ns, 5 ns for that at 30 ns, 35 ns and 45 ns, 20 ns for that at 60 ns, 100 ns and 100 ns for that at 200 ns and 400 ns, respectively. (*d*) An enlarged plot of the n_e profile at 400 ns. (*e*) Temporal evolution of the non-uniformity parameters: $R_{max\ to\ min}$ and the $R_{HV\ to\ GND}$ (defined in equations (1) and (2)). The relative error for the $R_{max\ to\ min}$ and the $R_{HV\ to\ GND}$ is ∼40%.

Table 1. Levels of helium and argon in the CR model.

Helium levels		$2\,^3S$	$2\,^1S$	$2\,^3P$	$2\,^1P$	$3\,^3S$	$3\,^1S$	$3\,^3P$	$3\,^3D$	$3\,^1D$	$3\,^1P$
Energy (eV)		19.82	20.62	20.96	21.22	22.72	22.92	23.01	23.07	23.07	23.07
	Argon Levels 1s (Paschen's notation)				$1s_5$	$1s_4$	$1s_3$	$1s_2$			
	Energy (eV)				11.55	11.62	11.72	11.83			
Argon Levels 2p (Paschen's notation)		$2p_{10}$	$2p_9$	$2p_8$	$2p_7$	$2p_6$	$2p_5$	$2p_4$	$2p_3$	$2p_2$	$2p_1$
Energy (eV)		12.91	13.08	13.10	13.15	13.17	13.27	13.28	13.30	13.33	13.48

atom population transfer,

$$\begin{aligned} &\mathrm{He_g + He}_i \leftrightarrow \mathrm{He_g + He}_j \\ &\mathrm{Ar_g + He}_i \rightarrow \mathrm{He_g + Ar^+} \\ &\mathrm{Ar_g + Ar}_i \leftrightarrow \mathrm{Ar_g + Ar}_j \end{aligned} \tag{4}$$

ionization,

$$\begin{aligned} &\mathrm{e + He}_i \rightarrow \mathrm{e + e + He^+} \\ &\mathrm{e + Ar}_i \rightarrow \mathrm{e + e + Ar^+} \end{aligned} \tag{5}$$

radiation and radiation trapping,

$$\begin{aligned} &\mathrm{He}_i \rightarrow \mathrm{He}_j + h\nu \\ &\mathrm{Ar}_i \rightarrow \mathrm{Ar}_j + h\nu \\ &\mathrm{Ar}_i \rightarrow \mathrm{Ar_g} + h\nu \\ &\mathrm{Ar_g} + h\nu \rightarrow \mathrm{Ar}_i \end{aligned} \tag{6}$$

three-body association,

$$\begin{aligned} &\mathrm{e + e + He^+} \rightarrow \mathrm{e + He}_i \\ &\mathrm{e + He_g + He^+} \rightarrow \mathrm{He_g + He}_i \\ &\mathrm{e + e + Ar^+} \rightarrow \mathrm{e + Ar}_i \\ &\mathrm{e + Ar_g + Ar^+} \rightarrow \mathrm{Ar_g + Ar}_i \end{aligned} \tag{7}$$

association and recombination processes involving excimers and excimer ions,

$$\begin{aligned} &\mathrm{He^+ + He_g + He_g} \rightarrow \mathrm{He_2^+ + He_g} \\ &\mathrm{He}_i \mathrm{+ He_g + He_g} \rightarrow \mathrm{He_2^* + He_g} \\ &\mathrm{e + He_2^+} \rightarrow \mathrm{He}_i \mathrm{+ He_g} \\ &\mathrm{Ar^+ + Ar_g + Ar_g} \rightarrow \mathrm{Ar_2^+ + Ar_g} \\ &\mathrm{Ar}_i \mathrm{+ Ar_g + Ar_g} \rightarrow \mathrm{Ar_2^* + Ar_g} \\ &\mathrm{e + Ar_2^+} \rightarrow \mathrm{Ar}_i \mathrm{+ Ar_g} \end{aligned} \tag{8}$$

Here, e are the electrons. $\mathrm{He_g}$, $\mathrm{He^+}$and $\mathrm{He_2^+}$ are the helium ground-state atoms, the helium ions and the helium excimer ions, respectively. He_i and He_j are the helium atoms in excited states. $\mathrm{Ar_g}$, $\mathrm{Ar^+}$, $\mathrm{Ar_2^+}$ are the argon ground-state atoms, the argon ions and the argon excimer ions, respectively. Ar_i and Ar_j are the argon atoms in excited states. Their respective cross sections and the rate coefficients are from [19–23].

Notice that for the helium $n = 3$ and the argon 2p levels, the radiation trapping is not included in the above processes, as the collisional broadening is strong and the self-absorption is weak. However, for the argon resonance states ($1s_2$, $1s_4$), the radiation trapping needs to be included and a plasma dimension Λ (taken as the radial dimension of the discharge, ~0.1 mm) is introduced to estimate its effect in the rate balance equation [20].

The rate balance equation for the excited states is

$$\frac{\mathrm{d}n_\mathrm{i}}{\mathrm{d}t} = f\left(n_\mathrm{g}, n_\mathrm{e}, n_\mathrm{i}, T_\mathrm{e}, T_\mathrm{g}, \Lambda\right), \tag{9}$$

f includes all the processes described above and is a function of gas density, electron density, excited states density, electron temperature, gas temperature and plasma dimension.

For the time period of interest (after ~8 ns), the $\mathrm{d}n_\mathrm{i}/\mathrm{d}t$ term (in equation (9)) for the helium $n = 3$ and the argon 2p levels is negligible. This can be justified by comparing this term with the ground-state excitation due to the electron impact,

$$R = \frac{\mathrm{d}n_\mathrm{i}/\mathrm{d}t}{n_\mathrm{e} n_\mathrm{g} Q_{\mathrm{g}\rightarrow\mathrm{i}}} \sim \frac{\mathrm{d}I_\mathrm{i}/\mathrm{d}t}{A_\mathrm{i} n_\mathrm{e} n_\mathrm{g} Q_{\mathrm{g}\rightarrow\mathrm{i}}} = \frac{\mathrm{d}(\mathrm{ln}I_\mathrm{i})/\mathrm{dt}}{\underline{n_\mathrm{e} n_\mathrm{g} Q_{\mathrm{g}\rightarrow\mathrm{i}}}} \tag{10}$$

Here, $Q_{\mathrm{g}\rightarrow\mathrm{i}}$ is the rate coefficient of the electron-impact excitation from ground state and A_i is the Einstein coefficient. Using the measured $\mathrm{d}(\mathrm{ln}I_\mathrm{i})/\mathrm{dt}$, n_e and n_g, and the values of n_i and T_e estimated from the steady-state model, one can show that the value of R is much smaller than one (<0.01). Therefore, the evolution of these excited levels can be considered as in the quasi-steady state,

$$f_\mathrm{j}\left(n_\mathrm{g}, n_\mathrm{e}, n_\mathrm{i}, T_\mathrm{e}, T_\mathrm{g}, \Lambda\right) = 0, \tag{11}$$

where j represents all the relevant species. By solving these equations with n_g, n_e, T_e, T_g and Λ as input parameters, n_i can be obtained. The T_e can then be obtained by the best fit of the measured line ratio with that from the model, with other parameters held constant.

However, in the initial breakdown phase (before ~5 ns), the emission intensity increases drastically with time, so it may be incorrect to assume the ratio R to be much less than unity during that time period. In this case, the steady-state CR model is no longer valid.

Even though the T_e reported in this work is obtained from the model including all the processes in the list, a simple analysis will help us to understand how the T_e dependence comes into play in the line ratio. When the n_e is higher than $10^{15}\,\mathrm{cm}^{-3}$ and the T_e is much higher than the T_g, the processes involving the electron-impact dominate over other processes (such as the population transfer of excited states due to atomic collisions, radiation and recombination, etc). In this case, we only need to consider the processes in equations (3) and (5) and the rate balance equation can be simplified as

$$\begin{aligned} &n_\mathrm{e} n_\mathrm{g} Q_{\mathrm{g}\rightarrow i} + n_\mathrm{e} \sum_{k\neq i} n_\mathrm{k} Q_{k\rightarrow i} \\ &= \left(n_\mathrm{e} \sum_{k\neq i} Q_{i\rightarrow k} + n_\mathrm{e} Q_{i\rightarrow\mathrm{ion}}\right) n_\mathrm{i} \end{aligned} \tag{12}$$

from which, we get,

$$n_\mathrm{i} = \frac{n_\mathrm{g} Q_{\mathrm{g}\rightarrow i} + \sum\limits_{k\neq i} n_k Q_{k\rightarrow i}}{\sum\limits_{k\neq i} Q_{i\rightarrow k} + Q_{i\rightarrow\mathrm{ion}}}. \tag{13}$$

Here, $Q_{k\rightarrow i}$ and $Q_{i\rightarrow k}$ are rate coefficients of the electron population transfer between the excited levels. $Q_{i\rightarrow\mathrm{ion}}$ is the rate coefficient of stepwise ionization. Using equation (13) for

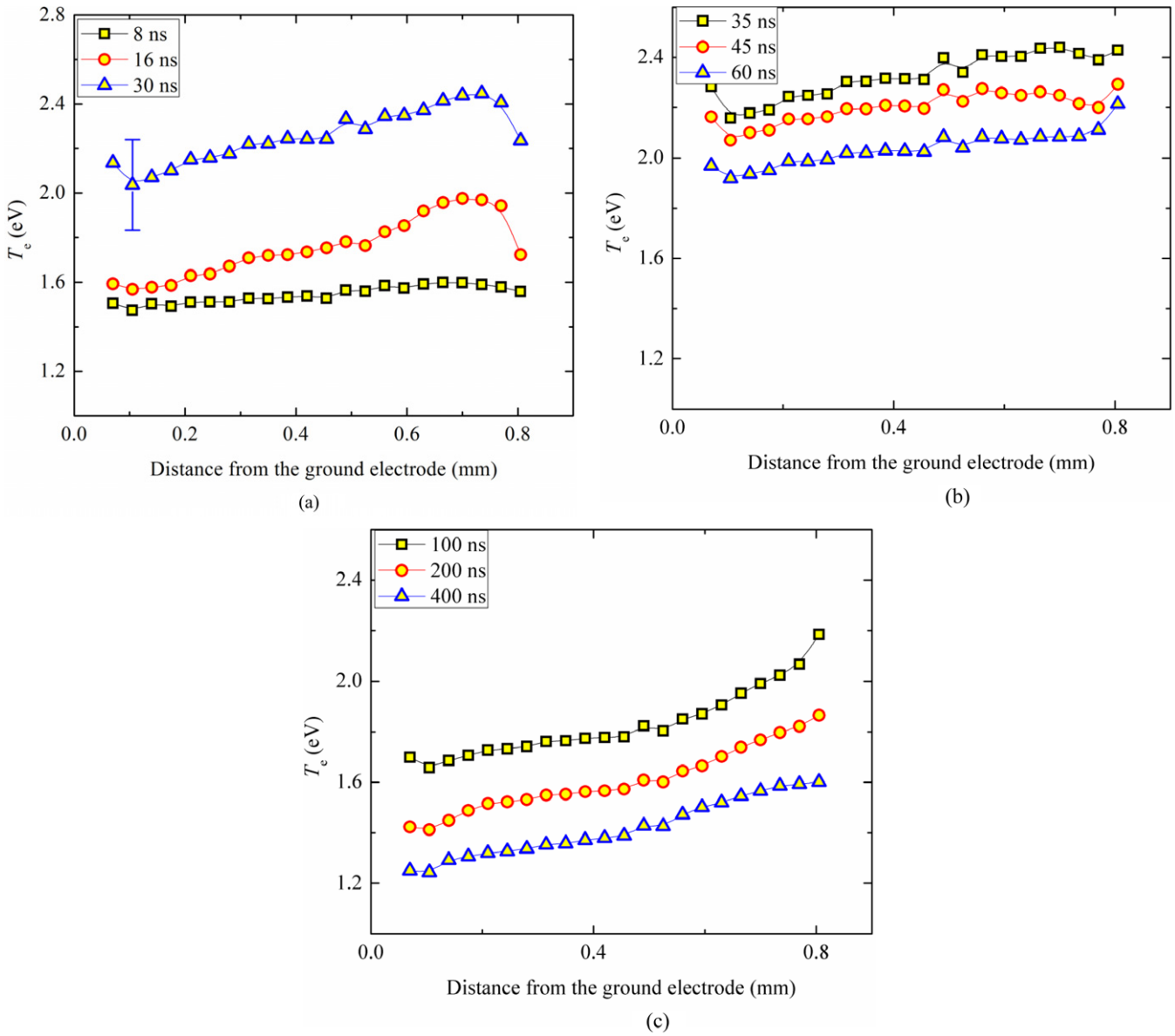

Figure 5. Temporal–spatial evolution of the electron temperature. The gate widths of the ICCD are the same as in figure 4.

both the helium 3 ^{3}D level and the argon 2p$_1$ level, we get

$$\frac{n_{\mathrm{He}}(3^3\mathrm{D})}{n_{\mathrm{Ar}}(2\mathrm{p}_1)} = \frac{(n_{\mathrm{g}}Q_{\mathrm{g}\to i} + \sum_{k\neq i} n_k Q_{k\to i})|_{\mathrm{He}}}{\left(n_{\mathrm{g}}Q_{\mathrm{g}\to i} + \sum_{k\neq i} n_{\mathrm{k}} Q_{k\to i}\right)\Big|_{\mathrm{Ar}}} \times \frac{(\sum_{k\neq i} Q_{i\to k} + Q_{i\to \mathrm{ion}})|_{\mathrm{Ar}}}{\left(\sum_{k\neq i} Q_{i\to k} + Q_{i\to \mathrm{ion}}\right)\Big|_{\mathrm{He}}}. \quad (14)$$

Notice that, in equation (14), the rate coefficients $Q_{k\to i}$, $Q_{i\to k}$and $Q_{i\to \mathrm{ion}}$ have relatively weak dependence on the T_e. For both of these two levels, the T_e dependence mainly comes from $Q_{\mathrm{g}\to \mathrm{i}}$(electron excitation from the ground state) and n_k, which are mainly $n = 2$ levels for helium and 1s levels for argon. Since the energy difference between these levels for both helium and argon is large (>7 eV), the ratio in equation (14) is sensitive to the variation of the T_e. Meanwhile, this equation also tells us that the ratio is quite insensitive to the variation of the n_e. Actually, one order of magnitude change in the value of the n_e will only result in a very small change in the T_e value (~0.1 eV).

3.3.2. The T_e evolution. The temporal–spatial evolution of the T_e is shown in figures 5(*a*)–(*c*).

In figure 5(*a*), at 8 ns, the T_e is very uniform with a value ~1.5 eV across the two electrodes. This is the initial stage of the multiplication process and the electron density is relatively low (figure 4(*a*)). At 16 ns, the T_e starts to increase with a small peak (~2 eV) near the HV electrode (about 0.1 mm away), indicating the region with the strongest heating. Notice that this also corresponds to the location of the peak value of the n_e (figure 4(*a*)). At 30 ns, the maximum T_e is reached (~2.4 eV), this is due to the continuous power absorption by the electrons from the external field.

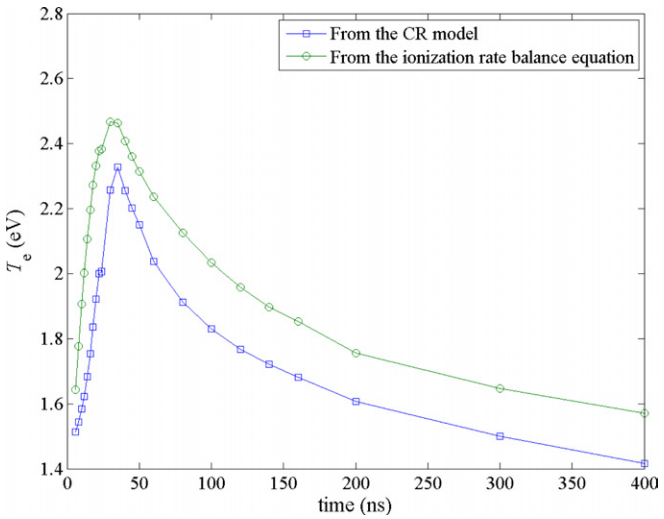

Figure 6. Temporal evolution of the volume-averaged T_e obtained from both the CR model and the ionization rate balance equation.

With the pulse off, the T_e starts to decrease at 35 ns (figure 5(*b*)) and it becomes more uniform than earlier times. The decrease of the T_e indicates the loss of high-energy electrons. However, comparing the T_e profile at 60 ns (figure 5(*b*)) with that at 100 ns (figure 5(*c*)), it can be seen that the rate of decrease differs with locations. The electron temperature near the HV electrode decreases much slower than that near the ground electrode, creating a monotonically increasing profile with location. The shape of this non-uniform profile remains almost unchanged for several hundred nanoseconds (figure 5(*c*)).

Furthermore, we estimated the volume-averaged T_e from the volume-averaged rate balance equation of the electrons,

$$\frac{dn_e}{dt} = n_e n_g Q_{iz} + \sum_k n_e n_k Q_{\text{step-iz}} - n_e^2 n_{ion} Q_{\text{3-body-a}} - n_e n_{ion} n_g \times Q_{\text{3-body-b}} - n_e n_{\text{excimer-ion}} Q_{\text{recomb}}, \quad (15)$$

where n_e, n_g, n_k, n_{ion} and $n_{\text{excimer-ion}}$ are the density of electron, atom in ground state and atom in excited states, ion and excimer ion, respectively; Q_{iz} is the rate coefficient of the ground-state ionization, $Q_{\text{step-iz}}$ is that of step-wise ionization, $Q_{\text{3-body-a}}$ and $Q_{\text{3-body-b}}$ are the rate coefficients of three-body association processes in equation (7) and Q_{recomb} is the rate coefficient of the recombination processes with excimer ions in equation (8). If we assume the electron density is in a quasi-steady state, an electron temperature can be estimated from equation (15).

Figure 6 shows the comparison of the volume-averaged T_es obtained from both the CR model and the rate balance equation. Considering the error in measurement and the uncertainty of the rate coefficients in both models, these two values agree with each other fairly well.

In the so called late afterglow period, the external power still provides the dominant heating process, even though its value (∼0.2 kW, or ∼5 × 10^{25} eV cm^{-3} s^{-1} during 100 to 200 ns) is much lower than the peak power during the pulse-on phase (∼106 kW at ∼6 ns). It is this power which provides a balance against the elastic and inelastic collisional energy loss and causes a slow decay rate of the electron temperature in the afterglow. A rough estimate indicates that, during the time between ∼100 ns and ∼400 ns, the heating due to the collisional processes (three-body recombination, super elastic collision with excited states, super elastic collision with dimers and Penning processes) is much weaker than the heating due to the external power in this discharge.

3.4. Limitation of the results

3.4.1. H_α versus H_β. The n_e shown in figure 4 comes from the Stark broadening of the H_α line as it has a satisfactory signal-to-noise ratio in the discharge under investigation. Ideally, we prefer to use the H_β line for the determination of the n_e, as it is insensitive to the variation of the T_e in the range of ∼1 to 3.5 eV [24, 25]. However, under the above discharge condition, the intensity of the H_β line is too weak to have a reasonable signal-to-noise ratio. This is the reason why we use the H_α line instead. Since the n_e obtained this way depends on the electron temperature and its value changes with both location and time, we need to estimate the introduced uncertainty in the value of the n_e. In order to do so, another atmospheric pressure discharge is generated with helium mixed with 1% hydrogen. In this discharge, the emission from both the H_α and H_β line can be collected with satisfactory signal-to-noise ratio, so the Stark broadening from both lines can be compared.

Figure 7(*a*) shows a typical measured spectral profile of the H_β line and the fitted one, which is obtained by the convolution of van de Waals broadening (Lorentzian), instrument broadening (Gaussian) and Stark broadening (Lorentzian). The uncertainty in electron density obtained by this fitting is less than 20%, considering all the error contributing factors [17, 24]. Figure 7(*b*) shows a typical pair of both the measured and fitted H_α line profiles, suggesting a good fit can also be achieved.

The comparison between the results from both the H_α and H_β lines is shown in figure 8. It can be seen that, for most of the data points, the difference between the two n_es is within 30%, even though a 50% discrepancy can be found at certain points. Considering the error bars in both measurements, the agreement between the two n_es is quite good. In addition, the current and voltage waveforms of these two discharges are almost identical to each other (not shown). Therefore, it is reasonable to assume that, for both gas mixture discharges at atmospheric pressure, the range of variation in either n_e or T_e is about the same, even though the discharge evolution time scale may be different due to the presence of molecular gases. Therefore, the Stark broadening of the H_α line can be used to estimate the n_e under the current discharge condition and the influence of the T_e does not have a significant effect on the determination of the n_e profile evolution during the entire discharge period.

3.4.2. Limitation of the CR model. In the CR model, a Maxwellian distribution for the electron energy is assumed during all the phases and at all locations of this discharge. However, this may not be true and the electron temperature discussed in this work may only represent the 'slope' of the high-energy electron distribution, which can be 'elevated'

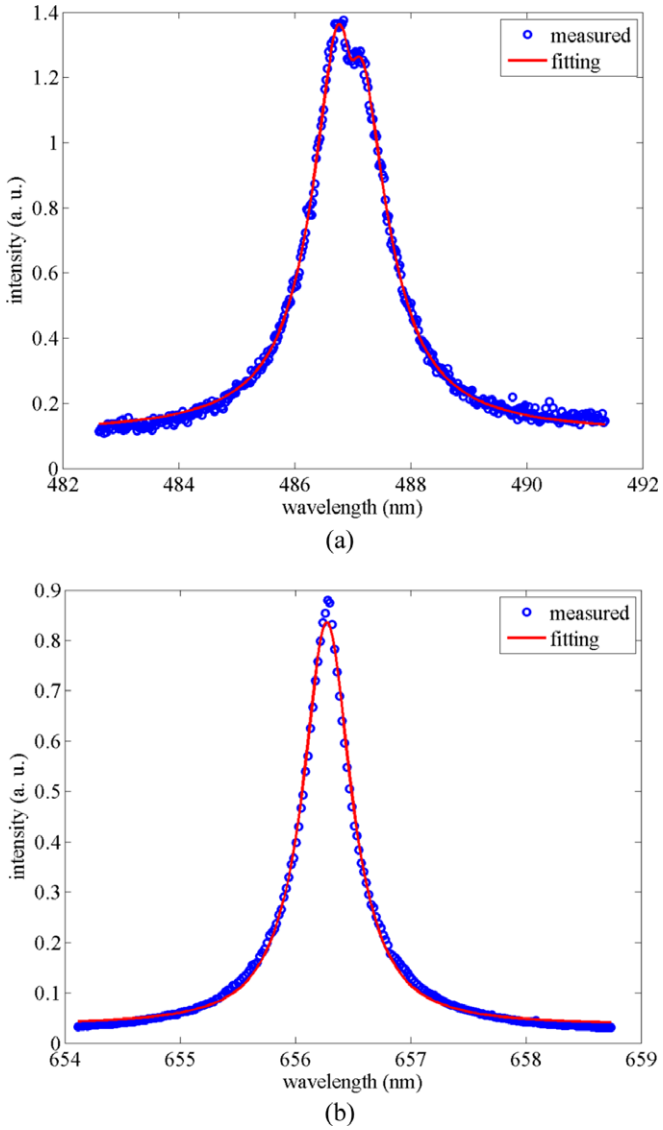

Figure 7. (*a*) Voigt fitting (with a central dip) of the H_β line measured during 50–70 ns at the position of 0.7 mm from the ground electrode. (*b*) Voigt fitting of the H_α line at the same time and position.

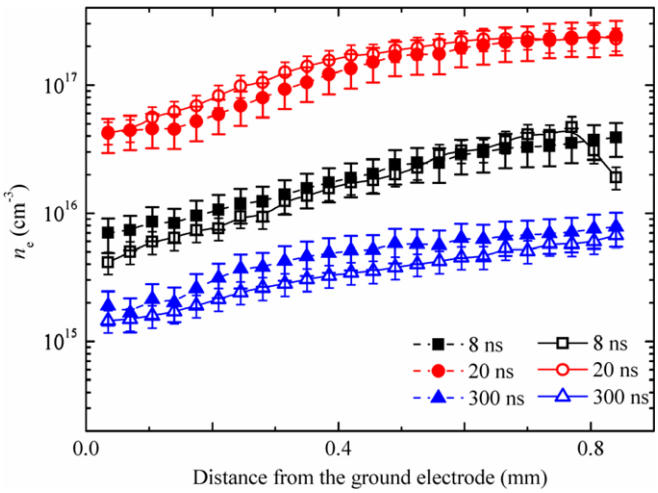

Figure 8. The comparison of the n_e from the Stark broadening of the H_α (filled scatters) and H_β lines (open scatters) at different time. The gate widths of ICCD for 8 ns, 20 ns and 300 ns are 2 ns, 2 ns and 100 ns, respectively.

during the pulse-on phase, driven by the external field and can be significantly 'depressed' in the afterglow due to strong inelastic collisions.

In fact, the time we start to apply the CR model is ∼8 ns after the breakdown (in the voltage falling phase), which is two orders of magnitude longer than the energy relaxation time of electrons with energy in the range of ∼0.1 to ∼1000 eV (below 0.1 ns) under the experimental condition. In this time period, it is unlikely to form a beam-like EEDF, so we assume the EEDF is a Maxwellian. This assumption should to be verified either by accurate measurement of the EEDF (by using Thomson scattering [26]) or by solving the Boltzmann equation, however, both of which are beyond the scope of this work.

Another source of uncertainty of this CR model comes from the recombination and association processes (equations (7) and (8)). These processes can be a significant source for the population of excited species when the T_e is low (comparable with the T_g) [27]. In order to account for these processes accurately in the CR model, one needs to know their rate coefficients for each excited level n_i, as well as the density of each ion for this gas mixture discharge. In this work, some estimated coefficients have been used [20]. As a result, this is a source of error in the obtained T_e. However, during the time period of interest (8–400 ns), the electron temperature is always much higher than T_g, so the main contribution to the generation of excited species is always electron-impact excitation. Therefore, the error introduced by these processes in the CR model should not be very large. In fact, we find the change of the obtained T_e is always within ∼0.2 eV under some extreme conditions.

3.4.3. The discharge geometry. The real discharge has a 3D structure and all the 'spatially resolved' measurements are done with the optical imaging system through the quartz window. This means the collected emission intensity is the integration over the 'cross section' of the discharge column. In this work, the 'radial' distribution of the discharge column is ignored and we only focus on the axial variation of the plasma parameters.

Gas temperature is an important parameter since its value is needed for the determination of van de Waals broadening and some of the collisional processes in the CR model. In this work, a constant gas temperature (∼500 K) is assumed across the discharge region during all the phases of the discharge. This T_g value is estimated from the rotational temperature (T_r) of the N_2 second positive band ($C\,^3\Pi_u, \nu = 0 \rightarrow B\,^3\Pi_g, \nu' = 0$, 335.5–337.5 nm) [28, 29], whose emission is collected from the discharge with 99% helium and 1% nitrogen gas mixture at atmospheric pressure. Even though the gas compositions are different, we assume the value of the T_g will not be very different for these nanosecond discharges. However, it is possible that the He+1%N_2 discharge has a higher T_g than the He+1%Ar case, since the former has more molecular gas and the ∼500 K is more likely an upper limit of the T_g.

On the other hand, it is questionable that whether this rotational temperature is a good estimate of the gas temperature under our condition [6]. The gas temperature may also change with time and location. However, all the above considerations are not of serious concern in this work. This is because the van de Waals broadening is much smaller than the Stark broadening due to high electron density during the time period of interest [15]. Therefore, the influence of the T_g on the n_e determination is negligible. Meanwhile, as mentioned in section 3.4.2, the recombination and association processes are not critical in the CR model and the influence of the gas temperature on the T_e estimation is also not important.

However, it is our opinion that although all of the arguments made in this work and the interpretations of the data are plausible, a more detailed analysis with a PIC/fluid model is needed to verify the assumptions and statements made here. With such a model, it is also possible to reveal more interesting features of the discharge physics.

4. Conclusion

In this work, we investigate the temporal and spatial evolution of the electron density and temperature in a nanosecond microdischarge with a pin-to pin electrode configuration, using the Stark broadening and collisional–radiative model. The evolution of the n_e profile can be divided into three phases with different characteristics: (1) during the initial breakdown period, the profile becomes more non-uniform with time under the influence of strong external electric field, the dominant process is ionization; (2) during the early afterglow period, the profile starts to relax to a more uniform one, the dominant process is diffusion; (1) during the late afterglow period the voltage at the HV electrode changes from positive to negative and the profile starts to develop a peak near the HV electrode. This is possibly due to the impact of energetic ions onto the HV electrode and emission of secondary electrons. As for the evolution of the T_e profile, during the pulse-on period, its behaviour is similar to that of the n_e, even though its value does not change as much. In the afterglow period, the residue external power input tends to slow down the electron cooling, especially in the region near the power electrode.

Acknowledgments

We are grateful for the enlightening discussions with Dr F Iza, Professors U Czarnetzki and J K Lee and Dr V Kolobov. This work is supported in part by the National Natural Science Foundation of China (Nos 11075093 and 10935006).

References

[1] Lissovski A A and Treshchalov A B 2009 *Phys. Plasmas* **16** 123501
[2] Treshchalov A B and Lissovski A A 2010 *Quantum Electron.* **40** 234–40
[3] Walsh J L and Kong M G 2007 *Appl. Phys. Lett.* **91** 251504
[4] Bruggeman P, Walsh J L, Schram D C, Leys C and Kong M G 2009 *Plasma Sources Sci. Technol.* **18** 045023
[5] Bruggeman P, Verreycken T, González M Á, Walsh J L, Kong M G, Leys C and Schram D C 2010 *J. Phys. D: Appl. Phys.* **43** 124005
[6] Wang Q, Doll F, Donnelly V M, Economou D J, Sadeghi N and Franz G F 2007 *J. Phys. D: Appl. Phys.* **40** 4202–11
[7] Lazzaroni C, Chabert P, Rousseau A and Sadeghi N 2010 *Eur. Phys. J.* D **60** 555–63
[8] Wang Q, Koleva I, Donnelly V M and Economou D J 2005 *J. Phys. D: Appl. Phys.* **38** 1690–7
[9] Mohr S, Du B, Luggenhölscher D and Czarnetzki U 2010 *J. Phys. D: Appl. Phys.* **43** 295201
[10] Du B, Sadeghi N, Tsankov T V, Luggenhölscher D and Czarnetzki U 2012 *Plasma Sources Sci. Technol.* **21** 045015
[11] Balcon N, Aanesland A and Boswell R 2007 *Plasma Sources Sci. Technol.* **16** 217–25
[12] Torres J, Palomares J M, Sola A, van der Mullen J J A M and Gamero A 2007 *J. Phys. D: Appl. Phys.* **40** 5929–36
[13] Zhu X M, Chen W C and Pu Y K 2008 *J. Phys. D: Appl. Phys.* **41** 105212
[14] Yarmolich D, Krasik Ya E, Stambulchik E, Bernshtam V, Yoon J K, Herrera B, Park S-J and Eden J G 2009 *Appl. Phys. Lett.* **94** 011501
[15] El Sherbini A M, Hegazy H and El Sherbini Th M 2006 *Spectrochim. Acta* B **61** 532–9
[16] Harilal S S 2004 *Appl. Opt.* **43** 3931
[17] Zhu X M, Walsh J L, Chen W C and Pu Y K 2012 *J. Phys. D: Appl. Phys.* **45** 295201
[18] Zhu L-G, Chen W-C, Zhu X-M, Pu Y-K and Li Z-R 2009 *Rev. Sci. Instrum.* **80** 023105
[19] Wang Q, Economou D J and Donnelly V M 2006 *J. Appl. Phys.* **100** 023301
[20] Zhu X M and Pu Y K 2010 *J. Phys. D: Appl. Phys.* **43** 015204
[21] NIST 2008 Atomic Spectra Database http://physics.nist.gov/PhysRefData/ASD/index.html
[22] Lindinger W, Schmeltekopf A L and Fehsenfeld F C 1974 *J. Chem. Phys.* **61** 2890
[23] Alves L L, Gousse G and Ferreira C M 1992 *J. Phys. D: Appl. Phys.* **25** 1713
[24] Gigosos M A and Cardeñoso V 1996 *J. Phys. B: At. Mol. Opt. Phys.* **29** 4795–838
[25] Gigosos M A and González M Á 2006 *AIP Conf. Proc.* **876** 294
[26] Crintea D L, Czarnetzki U, Iordanova S, Koleva I and Luggenhölscher D 2009 *J. Phys. D: Appl. Phys.* **42** 045208
[27] Celik Y, Tsankov T V, Aramaki M, Yoshimura S, Luggenhölscher D and Czarnetzki U 2012 *Phys. Rev.* E **85** 056401
[28] Moon S Y and Choe W 2003 *Spectrochim. Acta* B **58** 249
[29] Choe W 2007 private communication